

NGTS Observations of Enhanced Nanoflare Activity in Fully Convective Stars Linked to Plasma Resistivity

Christopher Dillon (✉ cdillon06@qub.ac.uk)

Queen's University Belfast <https://orcid.org/0000-0003-2709-7693>

David Jess

Queen's University Belfast <https://orcid.org/0000-0002-9155-8039>

Mihalis Mathioudakis

Queen's University Belfast <https://orcid.org/0000-0002-7725-6296>

Chris Watson

Queen's University Belfast

James Jackman

Arizona State University

Peter Wheatley

University of Warwick

Michael Goad

University of Leicester

Sarah Casewell

University of Leicester

David Anderson

University of Warwick

Matthew Burleigh

University of Leicester

Samuel Grant

Queen's University Belfast <https://orcid.org/0000-0001-5170-9747>

Richard West

University of Warwick

José Vinés

Universidad de Chile

Article

Keywords: nanoflare activity, M-dwarf stars, MV stars

Posted Date: September 24th, 2021

DOI: <https://doi.org/10.21203/rs.3.rs-882520/v1>

License:  This work is licensed under a Creative Commons Attribution 4.0 International License.

[Read Full License](#)

1 NGTS Observations of Enhanced Nanoflare Activity 2 in Fully Convective Stars Linked to Plasma 3 Resistivity

4 C. J. Dillon^{1,*}, D. B. Jess^{1,2}, M. Mathioudakis¹, C. A. Watson¹, J. A. G. Jackman³,
5 P. J. Wheatley⁴, M. R. Goad⁵, S. L. Casewell⁵, D. R. Anderson⁴, M. R. Burleigh⁵,
6 S. D. T. Grant¹, R. G. West⁴, and J. I. Vines⁶

7 ¹Astrophysics Research Centre, School of Mathematics and Physics, Queen's University Belfast, Belfast, BT7 1NN,
8 UK

9 ²Department of Physics and Astronomy, California State University Northridge, Northridge, CA 91330, USA

10 ³School of Earth and Space Exploration, Arizona State University, Tempe, AZ, 85287, USA

11 ⁴Department of Physics, University of Warwick, Gibbet Hill Road, Coventry CV4 7AL, UK

12 ⁵School of Physics and Astronomy, University of Leicester, University Road, Leicester, LE1 7RH, UK

13 ⁶Departamento de Astronomia, Universidad de Chile, Casilla 36-D, Santiago, Chile

14 *cdillon06@qub.ac.uk

15 ABSTRACT

16 Previous examination of fully-convective M-dwarf stars highlighted unexplained enhanced rates of nanoflare activity. A potential explanation was linked to the helical turbulence dynamo which operates in fully convective stars. However, recent studies have found this helical dynamo does not appear significantly different to the Solar dynamo. The specific role the convective boundary plays on observed nanoflare rates, until now, was not known. Here we find evidence that fully convective M2.5V (and later) stars display greatly enhanced nanoflare rates compared with their pre-convective boundary counterparts. Importantly, the rate of nanoflare activity increases with increasing spectral sub-type, with nanoflares exhibiting greatly enhanced flaring rates via Sweet-Parker reconnection. This occurs more favourably at increased plasma resistivities experienced in these later MV stars, suggesting a direct interplay between the rate of nanoflare occurrence and the intrinsic plasma parameters. As such, nanoflare behaviour is likely to be unrelated to the behaviour of the local dynamo.

17 Introduction

Nanoflares are small-scale magnetic reconnection events, with individual energies around 10^9 times less than their large-scale counterparts, spanning between 10^{22} to 10^{25} ergs. Following magnetic reconnection, impulsive energy deposition heats the local plasma¹⁻³. This leads to the impulsive brightening of the plasma⁴, which is followed by a decrease in the emitted radiation due to subsequent plasma cooling. The e -folding time, τ , is the time taken for the flare luminosity to decrease by a factor $1/e$, with its magnitude governed by the underlying local plasma conditions, such as the efficiencies of evaporative, non-evaporative, conductive, and radiative cooling processes⁵. Solar and stellar flare energies are governed by a power-law relationship⁶. Here, the power-law exponent governs the frequency, dN/dE , of flaring events with an associated energy, E , through the relationship,

$$\frac{dN}{dE} \propto E^{-\alpha}, \quad (1)$$

18 where α represents the power-law index. The expected nature of the power-law relation for flares implies that low-energy flares
19 should be many times more frequent than larger events, and that small-scale events will become more energetically significant
20 as the power-law index, α , increases. As a result, the occurrence rates of nanoflares are expected to be orders of magnitude
21 more frequent than macroscopic flares. Indeed, nanoflare rates could be as high as several thousand per second over an entire
22 stellar surface^{7,8}, which would make them a considerable component of the stellar energy budget. As a result, nanoflares have
23 been theorised as a solution to a long standing energy problem in astrophysics; *the coronal heating paradox*.

24 This paradox is that the outermost layer of the solar atmosphere is millions of degrees hotter than preceding layers, with no
25 conclusive mechanism found to explain this heating⁹. Flares occur primarily in the corona¹⁰, so would be able to drive local
26 heating via in-situ magnetic reconnection. However, the occurrence of large-scale flaring events are too infrequent to supply

27 sufficient energy to the corona. Nanoflares, on the other hand, have been proposed as a series of small-scale impulsive events
 28 driving coronal heating that, as a consequence of their low individual energies, had been hither-to undiscovered – explaining
 29 why the source of coronal heating may have remained unobserved^{7,11–13}.

30 This potential holds for stellar atmospheres as well as for the Sun. While solar nanoflares have been a considerable topic
 31 of interest over the last 20 years, stellar nanoflares have been almost entirely unexplored – remaining stubbornly below the
 32 noise floor of observations, with their low energies precluding the identification of individual stellar nanoflare events. However,
 33 nanoflares exhibit statistical signatures that distinguish them from the quiescent background of a star, alongside characteristic
 34 quasi-periodic signatures^{8,14}. The statistical signatures manifest themselves as distinct offsets from the normal distribution
 35 expected of shot noise patterns, which can be benchmarked by studying successive intensity fluctuations of the stellar time
 36 series. The periodic signatures manifest as features present in Fourier spectral energy densities, namely spectral slopes, an
 37 associated ‘turning-point’ where the spectral slope begins, and clear peaks in the range 1 – 10 mHz. These techniques do not
 38 rely on the individual identification of nanoflare events, so can identify nanoflare activity in seemingly quiescent time series⁸.

39 Such techniques have been applied to time series of seemingly quiescent, fully convective M-dwarf stars, uncovering
 40 novel evidence of stellar nanoflare activity⁸. A combination of statistical and Fourier analyses were used to examine both
 41 observational lightcurves and synthetic time series with simulated nanoflare signals. This allowed for the diagnosis of underlying
 42 nanoflare activity rates in these stars, finding stellar nanoflare activity in an M3V and two M2.5V stars. Part of this evidence
 43 was heightened (with respect to previous solar and stellar investigations) power-law slopes when the nanoflare occurrence
 44 rates were plotted as a function of their underlying energy. These power-law slopes were in excess of $\alpha = 3$, meaning that
 45 nanoflare activity forms a significant component of the stars overall energy budget. Here, we develop and apply these proven
 46 statistical nanoflare analysis techniques to a wide range of M-type stars. We examine 5 stars for each spectral sub-type,
 47 consisting of M0V, M1V, M2V, M2.5V, M3V, and M4V, spanning either side of the predicted convective boundary, which
 48 recent studies have placed at approximately M2.1–2.3V¹⁵. We compare their statistical and Fourier properties to previously
 49 generated nanoflare simulations⁸ in order to determine the underlying nanoflare conditions and the effect of the convective
 50 boundary on the uncovered nanoflare properties.

51 Results

52 Statistical Analysis

53 We present two example histograms of statistical intensity fluctuations in Figure 1 for stars observed with the Next Generation
 54 Transit Survey (NGTS – see Methodology for a description of the observations). These are NGTS J052346.3-361114 (M0V
 55 spectral type; top panel) and NGTS J050423.8-373021 (M4V spectral type; lower panel), where each time series has been
 56 detrended, with resulting intensity fluctuations normalised by the associated standard deviation, σ_N . From Figure 1 it is clear
 57 that opposite ends of the included spectral types, which lie on either side of the predicted convective boundary, demonstrate
 58 distinctly different statistical signatures. The M0V star exhibits very weak and inconclusive nanoflare signatures, with minimal
 59 negative median offset of the histogram and no elevated intensity fluctuations at $\sim 2 \sigma_N$. On the contrary, the M4V star has a
 60 clear excess of $\sim 2 \sigma_N$ intensity fluctuations, in addition to a prominent negative offset of the median histogram occurrence.
 61 The signatures of the M4V star shown in Figure 1 are consistent with previous positive stellar nanoflare identifications⁸. The
 62 distinct increase of visible nanoflare signatures within the expected regime of full convection is a promising sign that the
 63 enhanced nanoflare rates are related to the underlying convective nature of the star.

64 These examples illustrated in Figure 1 clearly identify the vastly different nanoflare signatures present at either end of the
 65 investigated range of spectral sub-types. To better examine the change in nanoflare activity across the given spectral range (M0V
 66 – M4V), the derived properties were averaged according to their specific spectral type following bootstrap methods¹⁶. Traditional
 67 averaging of features that are dependent on the underlying stellar plasma conditions from multiple stars is challenging due to the
 68 unpredictability of the standard errors of the given parameters. Hence, bootstrapping techniques are used extensively throughout
 69 the physical sciences to better calculate confidence intervals for data following non-standard or unknown distributions^{17–19}.

Spectral Type	Median offset (σ_N)	Fisher Skewness	ζ ratio	Kurtosis
M0V	-0.040 ± 0.001	0.004 ± 0.002	1.740 ± 0.005	0.128 ± 0.010
M1V	-0.040 ± 0.001	0.008 ± 0.004	1.746 ± 0.008	0.180 ± 0.013
M2V	-0.030 ± 0.001	0.003 ± 0.011	1.766 ± 0.010	0.196 ± 0.037
M2.5V	-0.050 ± 0.000	0.019 ± 0.003	1.739 ± 0.004	0.227 ± 0.072
M3V	-0.050 ± 0.000	0.025 ± 0.004	1.750 ± 0.006	0.180 ± 0.017
M4V	-0.050 ± 0.000	0.051 ± 0.014	1.754 ± 0.010	0.267 ± 0.029

Table 1. Averaged characteristics of the statistical properties by each spectral type.

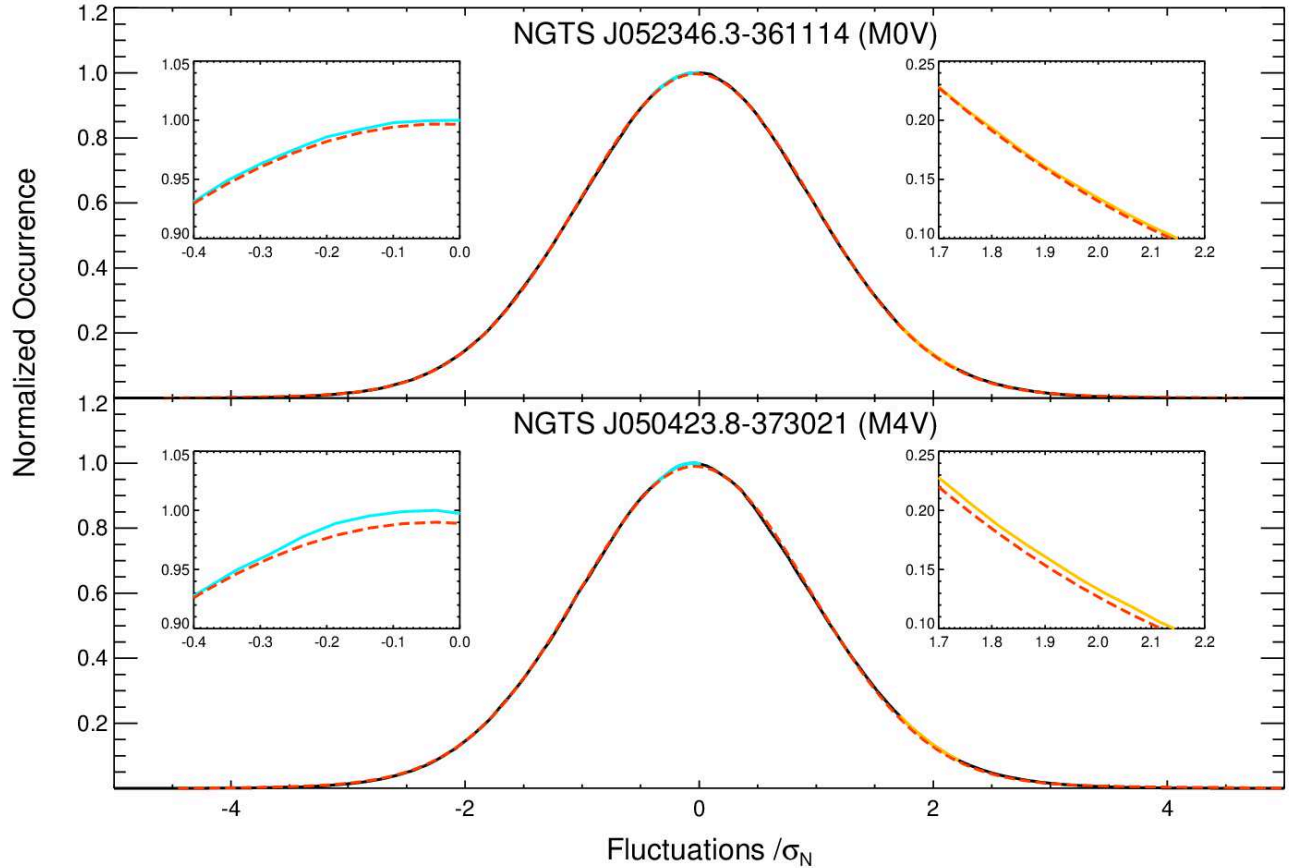


Figure 1. Histograms of intensity fluctuations, each normalised by their respective standard deviations, σ_N , for the NGTS J052346.3-361114 (M0V-type; top panel), and NGTS J050423.8-373021 (M4V-type; lower panel) lightcurves. A standardised Gaussian profile is overplotted in each panel using a dashed red line for reference. The M4V-type distribution has a negative median offset with respect to the Gaussian, in addition to elevated occurrences at $\sim 2 \sigma_N$, which is consistent with the statistical signatures of nanoflare activity. On the other hand, the M0V-type intensity fluctuations provide effectively zero negative median offset, and no elevated occurrences at $\sim 2 \sigma_N$. This is inconsistent with clear statistical signatures of nanoflare activity, with the resulting distribution remaining more consistent with the presence of photon-based shot noise. Zoomed insets highlight the ranges spanning $-0.4 \leq \sigma_N \leq 0.0$ and $1.7 \leq \sigma_N \leq 2.2$, where negative median offsets and occurrence excesses, respectively, are clearly visible for the M4V stellar source. For improved clarity, the blue and gold lines display the corresponding distributions in each zoomed panel.

70 Figure 2 shows the change in the median offset, kurtosis, Fisher skewness, and $\text{FW}_{\frac{1}{8}}\text{M-to-FWHM}$ ratio (hereafter, ζ) of the
 71 resulting histograms, respectively, as a function of spectral sub-type, with the results also tabulated in Table 1. From Figure 2,
 72 we find a distinct change in the nanoflare statistical signatures as a function of spectral sub-type, suggesting the convective
 73 boundary may play an important role in the generation of efficient nanoflare conditions. We find that M2.5V (and beyond) stars
 74 exhibit distinct nanoflare statistical signatures that are consistent with those put forward by previous research⁸. Specifically, the
 75 average median offset for the pre-M2.5V stars exhibits a large spread around a weakly offset value (upper panel of Figure 2),
 76 while the post-M2.5V stars demonstrate a larger consistent offset magnitude (with less uncertainty) of approximately $-0.05\sigma_N$.
 77 The Fisher skewness value is effectively zero for pre-M2.5V stars (second panel from bottom in Figure 2), suggesting no,
 78 or very weak, nanoflare activity. From M2.5V onward, there is a clear increasing trend in the Fisher skewness value of the
 79 fluctuation distribution, with the M4V sub-type displaying a Fisher skewness equal to 0.051 ± 0.014 , providing strong evidence
 80 for the presence of nanoflares.

81 The values of kurtosis (second panel from top in Figure 2) have a clear trend, whereby changes in spectral type from M0V
 82 to M4V produce increased levels of statistical kurtosis in the corresponding fluctuation distributions. It appears that the degree
 83 of statistical kurtosis is influenced directly by the spectral sub-type, with more fully-convective M4V stars demonstrating
 84 heightened levels of kurtosis compared with their M0V counterparts. It must be noted that the M3V sub-type does show a dip

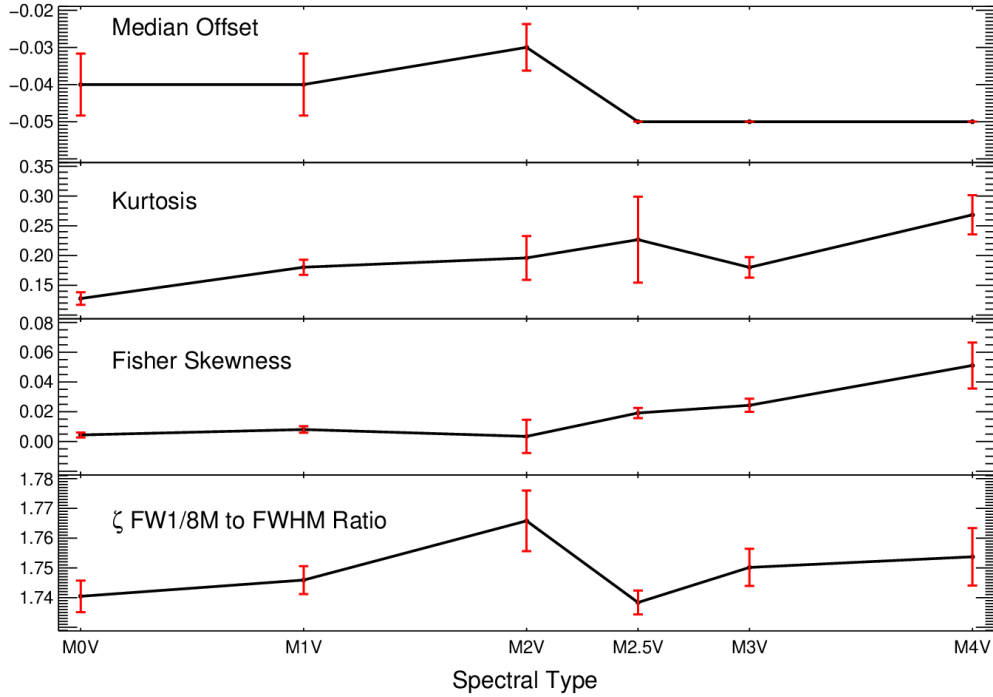


Figure 2. The bootstrap-averaged statistical properties of the intensity fluctuation histograms for each stellar classification. Beyond the convective boundary, at approximately M2.5V and later, sub-types begin to exhibit statistical signatures that are consistent with the presence of nanoflare activity, including larger median offsets (top panel), increasing levels of kurtosis (second panel from top), and higher Fisher skewness values (second panel from bottom). The ζ (FW $\frac{1}{8}$ M-to-FWHM ratio) values do not vary significantly as a function of stellar classification. However, this is likely due to the interplay between the power-law index of the nanoflares and the duration of the e -folding timescales, which are able to counteract the statistical effects of one another.

85 in its associated kurtosis value, which cannot presently be explained.

86 There is no clear trend visible in the corresponding ζ values (lower panel of Figure 2) as a function of spectral sub-type. It
 87 must be remembered that the ζ value is a measure of the deviation away from a standard Gaussian distribution, which has a
 88 value of $\zeta = 1.73$. Increased nanoflare decay timescales (i.e., larger τ values) result in broader tails of the intensity fluctuation
 89 distributions¹⁴, hence giving rise to $\zeta > 1.73$. On the contrary, large power-law indices help reduce the widths of the tails in the
 90 intensity fluctuation distributions due to the superposition of positive intensity fluctuations (e.g., new nanoflares) superimposed
 91 on top of decaying (i.e., negative) intensity fluctuations, which result in $\zeta < 1.73$. As such, the interplay between the power-law
 92 index and the nanoflare e -folding time produces the specific value of ζ measured. As such, the relatively consistent values of ζ
 93 found across the spectral range M0V – M4V may result from an increased nanoflare rate expected for M4V stars being negated
 94 by an increase in the associated decay timescales of the resulting nanoflares, i.e., a larger α term being coupled with longer τ
 95 values.

96 Comparing the intensity fluctuation statistical measurements (see, e.g., Table 1 and Figure 2) to those produced by Monte
 97 Carlo nanoflare simulations⁸, it is possible to estimate both the power-law index, α , and the nanoflare decay timescale, τ ,
 98 by establishing which combination of flare characteristics best matches the observational signatures. For pre-M2.5V stars,
 99 it was not possible to establish values for the power-law index and e -folding time that were self-consistent with the Monte
 100 Carlo models. For example, it was possible to find self-similarity between the observational and model power-law indices,
 101 but this resulted in decay timescales that were incompatible and inconsistent. As a result, we are unable to define nanoflare
 102 characteristics for pre-M2.5V stars, suggesting that nanoflare activity may be very weak (or not present) on these specific
 103 stellar sub-types. This strongly supports the intensity fluctuation distributions (see, e.g., the upper panel of Figure 1) where the
 104 fluctuations closely resemble shot noise patterns (i.e., absent of clear statistical nanoflare signatures).

105 The statistical parameters for the M2.5V, M3V and M4V stars, which are believed to be beyond the convective boundary
 106 and therefore best described as ‘fully convective’, exhibit values consistent with the power-law indices of $\alpha = 2.25 \pm 0.25$
 107 or $\alpha = 3.00 \pm 0.25$, $\alpha = 2.25 \pm 0.20$ or $\alpha = 3.00 \pm 0.20$, and $\alpha = 2.30 \pm 0.20$ or $\alpha = 3.10 \pm 0.20$, alongside the e -folding
 108 timescales of $\tau = 200 \pm 100$ s, $\tau = 200 \pm 100$ s, and $\tau = 450 \pm 50$ s, respectively (See Table 2_a). The approximate symmetry

(a) Nanoflare parameters per spectral type, derived from statistical properties of Monte-Carlo modelled nanoflare timeseries. The approximately symmetrical distribution of statistical properties leads to an ambiguity in the derived power-law indices, hence α_1 and α_2 .

Spectral Type	α_1	α_2	$\tau(s)$
M2.5V	2.25 ± 0.25	3.00 ± 0.25	200 ± 100
M3V	2.25 ± 0.20	3.00 ± 0.20	200 ± 100
M4V	2.30 ± 0.20	3.10 ± 0.20	450 ± 50

(b) Nanoflare parameters per spectral type, derived from Fourier properties of Monte-Carlo modelled nanoflare timeseries. There is no ambiguity in the derived power-law indices.

Spectral Type	α	$\tau(s)$
M2.5V	3.00 ± 0.15	200 ± 100
M3V	3.00 ± 0.15	250 ± 100
M4V	3.10 ± 0.15	450 ± 50

Table 2. Nanoflare parameters per spectral type, derived from statistical and Fourier properties of Monte-Carlo modelled nanoflare timeseries respectively.

of the statistical distributions about their peak values leads to ambiguity in the derived power-law indices. As a result, it is possible to map each sub-type onto two distinct solutions for the power-law index. Irrespective of this ambiguity, both sets of possible nanoflare conditions are highly active (i.e., $\alpha > 2$), in stark contrast to the effectively zero statistical nanoflare signals observed in the pre-M2.5V spectral sub-types. The increased uncertainties in the M2.5V power-law indices are due to the larger errors associated with the kurtosis values for these spectral sub-types. M2.5V stars are at the boundary of predicted full convection, so a larger spread in their nanoflare properties would be expected if full convection is the cause of the spectral ‘break’ in associated power-law indices.

Interestingly, the M4V stars display evidence for longer e -folding timescales and larger power-law indices when compared to their M2.5V and M3V counterparts. As discussed above, this is likely an explanation for the relatively constant ζ values throughout the spectral sub-type range, whereby the statistical effects of higher power-law indices are negated by the slower decay timescales associated with those stars, which is consistent with previous solar and stellar case studies^{8,14}.

Overall, the changes in the statistical parameters indicate that post-convective boundary M-dwarf stars (i.e., M2.5V and later) exhibit greatly enhanced stellar nanoflare activity when compared to the pre-convective boundary M-dwarfs that show little-to-no evidence for nanoflare activity.

Fourier Analysis

As with the statistical signatures shown in Figure 2, there are dramatic differences in the Fourier properties between M0V and M4V stars. As seen in the Power Spectral Density (PSD) plot of Figure 3, the M0V has an effectively flat power spectrum suggesting no nanoflare signal is present⁸ (i.e., remaining consistent with a shot noise distribution of intensity signals), which is contrasted by the M4V star that demonstrates a spectral slope of $\beta = -0.57 \pm 0.05$ between the frequencies $\sim 0.3 - 6.0$ mHz. In Figure 3, the black crosses represent the individual frequency-dependent power measurements, while the solid red line depicts a trendline established over ± 6 frequency elements (± 0.239 mHz). In the lower panel of Figure 3, a PSD slope is consistent with enhanced rates of stellar nanoflare activity, which begins at the ‘turning point’ of 0.32 ± 0.04 mHz. The turning point is defined as the initial Fourier peak before the gradual reduction in spectral power with increasing frequency⁸. It must be noted that both PSD plots shown in Figure 3 (i.e., for M0V and M4V spectral types) exhibit numerous power peaks in the range of 1 – 10 mHz, consistent with both stellar nanoflare signatures⁸ and the presence of p -mode oscillations generated in the convective layers of M-dwarf stellar sources, where M-dwarf stars are believed to exhibit solar-like oscillations, hence producing p -mode signatures synonymous with the typical solar frequency range^{20,21}. As the entire range of spectral types included in this study (M0V – M4V) are expected to exhibit p -mode oscillations, the peak frequencies within this interval are not conclusive evidence alone of nanoflare activity.

The averaged (following bootstrap procedures) Fourier properties per spectral type are shown in Figure 4, and tabulated in Table 3. As with the averaged statistical signatures shown in Figure 2, there is a marked change in Fourier features consistent with nanoflare activity for spectral classifications M2.5V and later. Evidence for this is shown in the averaged PSD spectral gradient (lower panel of Figure 4), where pre-M2.5V stars have relatively flat spectral slopes ($\beta \sim 0$), yet stellar sources beyond the convective boundary at M2.5V demonstrate increased magnitude spectral slopes in the range of $-0.6 \leq \beta \leq -0.3$. Note that the peak frequency values (upper panel of Figure 4) are relatively consistent across all M-dwarf stellar sources, approximately in the range of 2 – 4 mHz. As discussed above, this alone does not constitute evidence of nanoflare activity since all of these sources are expected to demonstrate p -mode oscillations spanning that particular frequency interval^{20,22}.

The corresponding ‘turning point’, where the spectral slopes are observed to begin, is, of course, equal to zero for the pre-M2.5V stars since they do not exhibit any associated spectral slopes (middle panel of Figure 4). However, for spectral classifications beyond M2.5V, where the stars are believed to be fully convective, a relatively constant value (when errors are included) in the range of $0.3 \leq f \leq 0.9$ mHz is found, which is consistent with previous nanoflare studies⁸. In simulated

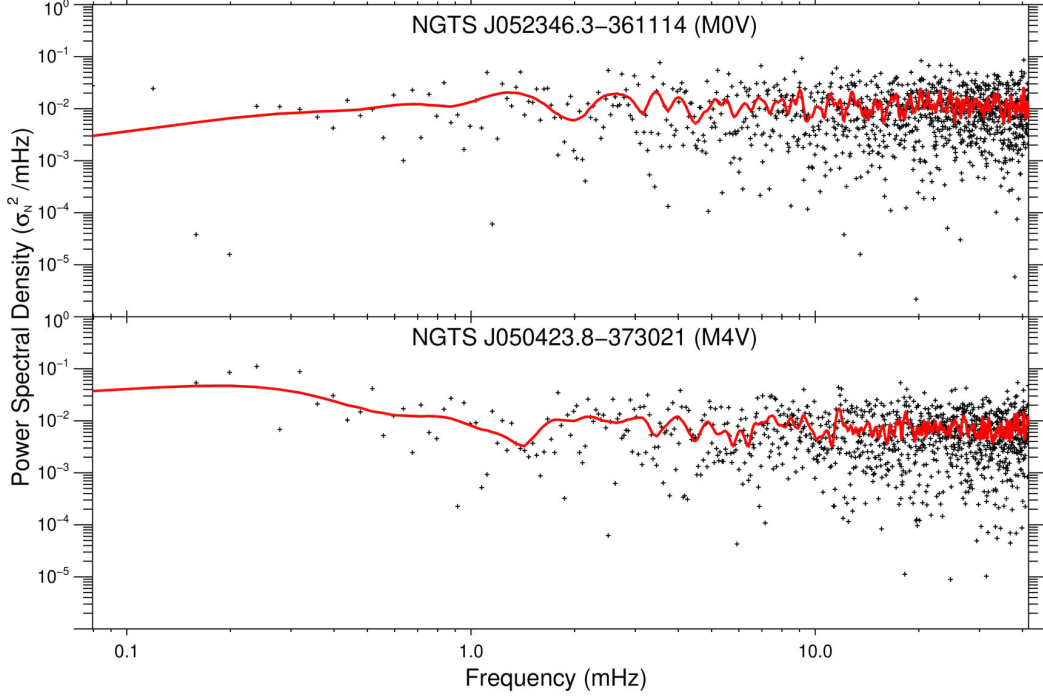


Figure 3. The Fourier power spectral densities (PSDs) for example M0V (upper panel) and M4V (lower panel) stellar sources, displayed in normalised units of σ_N^2/mHz . The crosses in each panel depict the individual power values as a function of frequency, while the solid red line reveals a trendline calculated over ± 6 frequency elements (± 0.239 mHz). It can be seen that the PSD for the M0V star is relatively flat, with small-amplitude power enhancements in the range 3 – 10 mHz, which is consistent with typical p -mode oscillations. On the contrary, the PSD for the M4V star exhibits a clear enhancement of spectral energy at lower frequencies, resulting in a spectral slope of $\beta = -0.57 \pm 0.05$ that begins at 0.32 ± 0.04 mHz, followed by numerous power peaks in the range of 1 – 10 mHz, which is consistent with the presence of both nanoflare activity and p -mode oscillations.

Spectral Type	Gradient	Turning Point (mHz)	Peak frequency (mHz)
M0V	$+0.044 \pm 0.023$	0.000 ± 0.000	3.952 ± 0.320
M1V	-0.051 ± 0.019	0.000 ± 0.000	2.695 ± 0.278
M2V	-0.035 ± 0.022	0.000 ± 0.000	1.956 ± 0.611
M2.5V	-0.326 ± 0.044	0.762 ± 0.105	1.821 ± 0.338
M3V	-0.330 ± 0.022	0.684 ± 0.063	3.276 ± 0.557
M4V	-0.518 ± 0.018	0.467 ± 0.103	1.757 ± 0.822

Table 3. Average characteristics of the Fourier PSD properties by each spectral type.

150 nanoflare lightcurves, an increased flare decay rate (i.e., a longer τ value) gives rise to a decrease in frequency of the Fourier
 151 turning point. Examination of the middle panel of Figure 4 shows that while the turning point frequencies are distinctly
 152 different from the pre-M2.5V stars, there does seem to be tentative evidence that the average turning point frequency decreases
 153 across the M2.5V, M3V, and M4V spectral types. This is further evidenced in Table 3, where the turning points of the M2.5V,
 154 M3V, and M4V stars are computed as 0.762 ± 0.105 mHz, 0.684 ± 0.063 mHz, and 0.467 ± 0.103 mHz, respectively. The
 155 evidence suggests that the e -folding timescales associated with the M4V stars are longer than their M2.5V counterparts, which
 156 is consistent with the intensity fluctuation statistical signatures discussed above.

157 Comparing the derived Fourier properties to the heat maps of simulated signatures shown in Figure 5, it is possible to
 158 estimate the power-law indices and decay timescales for each of the M2.5V, M3V, and M4V stellar types that show clear
 159 evidence for nanoflare activity. We find power-law indices of $\alpha = 3.00 \pm 0.15$, $\alpha = 3.00 \pm 0.15$, and $\alpha = 3.10 \pm 0.15$, alongside
 160 nanoflare e -folding timescales of $\tau = 200 \pm 100$ s, $\tau = 250 \pm 100$ s, and $\tau = 450 \pm 50$ s, for the M2.5V, M3V, and M4V spectral
 161 types, respectively (see Table 2_b). Importantly, these values are consistent with the statistical analyses, with the Fourier

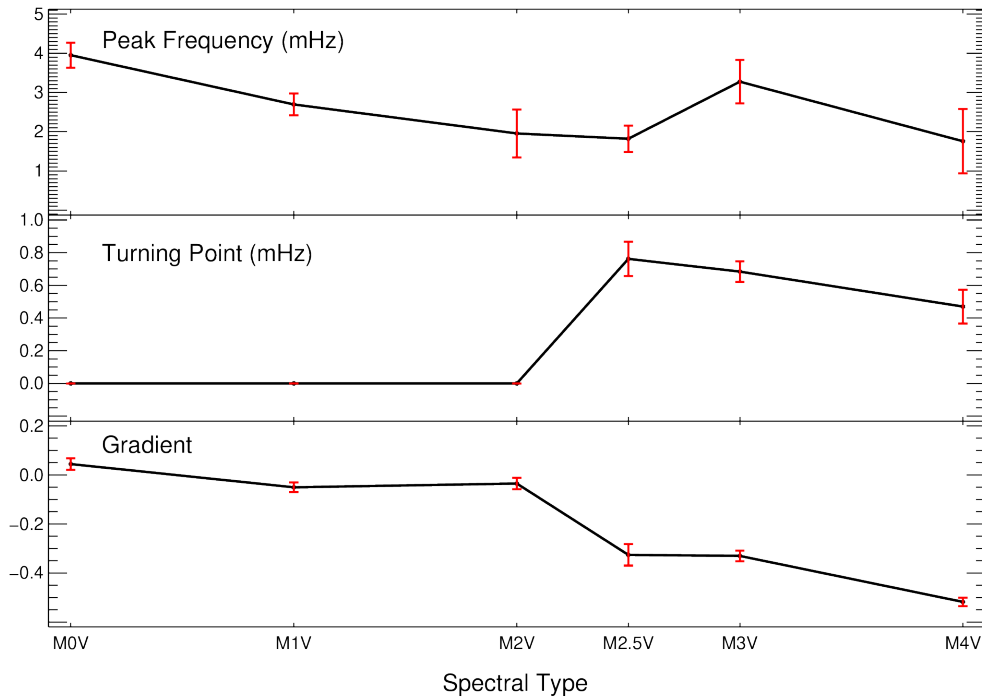


Figure 4. The bootstrap-averaged properties of the Fourier power spectral densities (PSDs) across each spectral type. The upper panel displays the peak frequency values (in mHz), which are found to reside within the range of approximately 1 – 4 mHz, which is consistent with both nanoflare activity and p -mode oscillations, and therefore cannot be used as an indicator of nanoflare activity by itself. The middle and lower panels display the turning point frequencies (in mHz) and subsequent spectral slopes, respectively, as a function of stellar classification. When compared to the Monte Carlo nanoflare simulation outputs depicted in Figure 5, the distinct jump in turning point frequency and spectral gradient at the convective boundary (M2.5V) provides clear evidence of prominent nanoflare activity in M2.5V – M4V stellar sources.

162 techniques providing additional benchmarks to validate the nanoflare properties extracted from the observational time series
 163 and resolve the ambiguity in power-law index arising from the statistical analysis. In contrast to the statistical mapping, the
 164 derived Fourier parameters of the M3V stars are consistent with a marginal e -folding time enhancement compared to the M2.5V
 165 classifications. This is likely related to the same physical processes that caused enhanced e -folding timescales in the M4V stars.
 166 However, this is difficult to ascertain due to the relatively large errors in determining the average plasma decay rates over the
 167 entire stellar surface.

168 Evidence of Enhanced Nanoflare Activity Rates in Fully Convective Stars

169 Combining the Fourier and statistical analyses, we find that the fully convective M2.5V and M3V sub-types exhibit nanoflare
 170 power-law indices of $\alpha = 3.00 \pm 0.20$ and $\alpha = 3.00 \pm 0.18$, respectively. The M2.5V sub-types are consistent with a decay
 171 timescale of $\tau = 200 \pm 100$ s, whereas the M3V stars display tentative evidence for a slightly enhanced e -folding timescale of
 172 $\tau = 225 \pm 100$ s (these values of α and τ derived from the combined statistical and Fourier analysis are tabulated in Table 4).
 173 These e -folding timescales and power-law indices are values consistent with similar M-dwarf spectral types⁸. The M4V stars
 174 exhibit elevated power-law indices of $\alpha = 3.10 \pm 0.18$, with an increased decay timescale of $\tau = 450 \pm 50$ s, which we believe
 175 may be related to Sweet-Parker reconnection processes.

176 Convection is a primary driver of magnetic reconnection in stars²³. As magnetic reconnection is the driving force behind
 177 flares, changes to the convective nature of a star have important implications for the resulting flare dynamics. Fully convective
 178 stars lack a tachocline, where the radiative interior of the star meets the convective exterior²⁴. The tachocline is believed to
 179 be responsible for the magnetic dynamo, hence driving magnetic reconnection processes in solar-like stars²⁵. In stars with a
 180 fully convective atmosphere, the dynamo is theorised to be driven by helical turbulence^{26–28}, but this change in dynamo is still
 181 under debate. Indeed, investigation into the relationship between stellar rotation and activity levels for fully-convective late
 182 M-type dwarf stars have found that the rotation/activity relationship for fully convective stars was almost indistinguishable
 183 from partially convective stars, suggesting the activity levels of fully convective stars may somehow be driven by a solar-like
 184 dynamo^{29,30}. As such, an alternative source for the enhancement of small-scale reconnection may be more likely. Small-scale

185 flaring has been shown to occur more favourably via Sweet-Parker reconnection³¹, and the rate of Sweet-Parker reconnection
 186 is inversely connected to the plasma Lundquist number, leading to enhanced nanoflaring in stars with low plasma Lundquist
 187 numbers. Fully convective stars are believed to host plasma with a higher resistivity value³², which lowers the associated
 188 plasma Lundquist numbers. If nanoflare rates are enhanced in fully convective stars, then investigating whether this is due to
 189 the change in dynamo, or down to the plasma resistivity, could answer important questions regarding the dynamo physics in
 190 operation in these stars, and consequently the nature of the solar dynamo.

191 Small-scale pico/nano-scale flares occur more favourably via Sweet-Parker than Petschek reconnection³¹. This would
 192 explain a discontinuity in the power-law relationship between nanoflares and their larger scale counterparts, which remain driven
 193 by Petschek-like reconnection³³. The Sweet-Parker reconnection process is inversely proportional to the square root of the
 194 plasma Lundquist number, which is itself inversely proportional to the plasma resistivity. As such, Sweet-Parker reconnection
 195 is more favourable in poorly conducting plasmas. The increased decay timescale of $\tau = 450 \pm 50$ s, alongside the associated
 196 increased power-law index of $\alpha = 3.10 \pm 0.18$, found for the M4V sub-type may be related to increased plasma resistivity,
 197 which matches expectations for mid-to-late M-dwarfs³². In contrast, pre-convective boundary (M0V – M2V) stars exhibit weak
 198 (if any) nanoflare signals, suggesting that fully convective stellar atmospheres lead to a large enhancement of nanoflare activity.

Spectral Type	α	$\tau(s)$
M2.5V	3.00 ± 0.20	200 ± 100
M3V	3.00 ± 0.18	225 ± 100
M4V	3.10 ± 0.18	450 ± 50

Table 4. Nanoflare parameters per spectral type, derived from combined statistical and Fourier properties of Monte-Carlo modelled nanoflare timeseries.

199 The enhanced small-scale flare rates in fully convective stars holds profound implications for the energy budgets of those
 200 stellar sources. The energy output of rapid and continuous nanoflares may be a major component of the overall stellar energy
 201 budget, yet are hidden within the noise envelope of the observations and can only be extracted through use of large-scale
 202 statistical and Fourier analyses. The question of whether the enhanced flaring visible in post-convective boundary M2.5V
 203 – M4V stars is due to the helical dynamo or altered plasma Lundquist conditions in these stars is an avenue to explore in
 204 future work. Furthermore, our work reveals evidence that M4V stars are linked to nanoflare events that have inherently longer
 205 decay timescales (i.e., larger τ values) as well as larger power-law indices. Importantly, mid M-dwarf sub-types should have
 206 decreased optical depths, alongside increased plasma resistivities, a trend which continues to late M9 sub-types³². If the
 207 nanoflare e -folding times continue to increase with increasing M-dwarf sub-type, it would support the scenario of increased
 208 plasma resistivity leading to increased small-scale flaring via Sweet-Parker reconnection. This would appear to support the
 209 findings of^{29,30}, that the stellar dynamo in these fully convective stars is not distinct from the solar-like dynamo. As a result, it
 210 is of paramount importance to source sufficient late M-type stellar time series for follow-up analyses.

211 Discussion

212 Evidence for stellar nanoflares has been observed on a further 15 post-convective boundary (M2.5V, M3V, and M4V classifica-
 213 tion) stars, with nanoflare power-law indices and e -folding times consistent with the enhanced rates of stellar nanoflare activity
 214 previously observed⁸. The marked increase in nanoflare activity is coincident with M2.5V and later sub-types, suggesting
 215 that the change from partial to fully convective atmospheres may be responsible. The post-convective boundary stars exhibit
 216 nanoflare rates that are enhanced from those seen at larger energies in other stars and the Sun, with power-law indices found to
 217 be in the region of $\alpha = 3.00 \pm 0.20$ for M2.5V and M3V sub-types, with slightly larger values of $\alpha = 3.10 \pm 0.18$ for M4V
 218 sub-types. The decay timescales for M2.5V and M3V stars were found to be on the order of $\tau = 200 \pm 100$ s, while evidence
 219 was presented for increased plasma e -folding times of $\tau = 450 \pm 50$ s in the M4V stars, suggesting the presence of Sweet-Parker
 220 reconnection processes.

221 On the contrary, pre-convective boundary M-dwarf (M0V, M1V, and M2V classification) stars exhibit little-to-no statistical
 222 or Fourier-based nanoflare signals, suggesting full convection is a requirement for enhanced nanoflare activity. Additionally,
 223 the underlying reason why fully convective atmospheres lead to enhanced nanoflare activity should be explored, i.e., is this
 224 due to an altered dynamo, or due to other plasma changes such as modification of the corresponding Lundquist number? The
 225 latter explanation is our leading theory, due to the altered plasma conditions we find, and the emerging evidence for solar-like
 226 behaviour in helical dynamos^{29,30}. One avenue of exploration would be examining M5V (and later) stellar types, to investigate
 227 if there is a continuing trend in the flare decay rate and associated power-law index, which could be linked to increasing plasma
 228 resistivity, and thus increased Sweet-Parker reconnection rates. It is likely such observations would need to be coupled to
 229 detailed theoretical and modelling efforts using well-developed numerical simulations^{34–37}.

230 It goes without saying that enhanced small-scale reconnection in fully convective stars may mean that nanoflare activity
231 could be a significant component of their overall energy budget. Large-scale multi-year studies of stellar nanoflare rates in
232 fully convective M-dwarfs would further our understanding of nanoflare behaviour across different activity cycles, which
233 would further shine light on the ubiquity and role nanoflares play in these dynamic host stars. This can be achieved through
234 further use of large-scale sky surveys (like the NGTS) and space-based observations from the likes of the Transiting Exoplanet
235 Survey Satellite (TESS)³⁸, alongside targeted campaigns using high-cadence observational platforms, such as HiPERCAM³⁹,
236 or multi-band photometry such as the Rapid Eye Mount (REM) telescope⁴⁰ to investigate the nanoflare signature across layers
237 of the Stellar atmosphere.

238 Methods

239 Observations With NGTS

240 To remain consistent with established stellar nanoflare analysis⁸, the Next Generation Transit Survey⁴¹ (NGTS) was utilised
241 to obtain the observations. The initial spectral classification generated by the NGTS pipeline, which utilises Spectral Energy
242 Distribution fitting⁴¹, was combined with stellar parameters from the TESS Input Catalog Version 8⁴², to ensure robust spectral
243 sub-type identification. The magnitude of the stars (spanning $\sim 12 - 14$), were chosen to match the previous stellar nanoflare
244 study⁸, ensuring similar noise statistics. The long timeseries (each in excess of 10^5 frames) and short cadence (~ 12 s) available
245 for thousands of M-type stars allow for the accumulation of suitable number statistics necessary for nanoflare analyses.

246 After accounting for magnitude considerations, avoiding blended sources, and ensuring TIC matching, we were able to find
247 5 stars for each spectral sub-type, consisting of M0V, M1V, M2V, M2.5V, M3V, and M4V. The stellar properties including
248 GAIA identifiers, RA, and Dec. of these stars can be found in Table 5. Only one suitable M5V star with TIC-derived stellar
249 parameters could be identified, and no sub-types later than this were found. The intrinsic brightness of M-dwarfs decreases
250 with increasing sub-type⁴³, leading to difficulty in identifying suitable candidate stars with the desired brightness properties.
251 Future investigations of post-M4V stars may be fruitful, but identifying a suitable number of candidates may prove difficult
252 with existing instrumentation. Hence, we limit our current study within the range of M0V – M4V, where we have multiple
253 candidates available for comparison. This range also overlaps well with the predicted convective boundary of M2.1–2.3V¹⁵,
254 making it suitable for the study of the role convection plays in the resulting nanoflare activity.

255 The lightcurves were background corrected and flat-fielded via the NGTS data reduction pipeline described in⁴¹. This
256 pipeline calculates a relative error in the flux at each data point in the time series. This error correlates with cloudy weather
257 and/or high airmass values. Any fluctuations in this error exceeding 1σ above the mean value were removed, resulting in
258 $\sim 10\%$ of each time series being omitted. This removed any data that had statistically significant increases in its associated flux
259 uncertainties, therefore preventing any large flux errors (largely due to poor seeing conditions) from contaminating the final
260 time series.

261 Next, the lightcurves extracted for each observing sequence were examined for the presence of macroscopic flare signatures
262 following the same methodology described by⁸. Specifically, to isolate and remove the macroscopic flares, each lightcurve
263 was searched for emission signatures exceeding 3σ above the mean value, lasting continually for a minimum of 1 minute
264 (5 datapoints). Based on a normal distribution, the probability of this occurring by chance is $\lesssim 2 \times 10^{-13}$, and hence allowed
265 for the robust detection of intensity fluctuations resulting from macroscopic flaring activity. Every star, apart from the
266 M2V candidate NGTS J062005.7-372555, demonstrated macroscopic flare signatures, resulting in the removal of a further
267 $\sim 0.2 - 2.5\%$ of the remaining M-type time series. The degree of macroscopic flare emission varied with the spectral sub-type,
268 with M4V stars exhibiting approximately five times more detected flares than the M0V stellar types. Such bias towards the
269 spectral sub-type is consistent with the studies of⁴⁴ and⁴³, where later MV sub-types were also found to exhibit increased
270 macroscopic flare activity. Previous examinations of (macroscopic) stellar flares on late-type MV stars have found power-law
271 indices in the range of $1.5 \leq \alpha \leq 2.7$ ^{11,44-51}, which are significantly below the nanoflare power-law index ($\alpha \approx 3.25$) found in
272 similar stars by⁸. As a result, it appears unclear whether a spectral ‘break’ in the power-law index occurs between large-scale
273 flares and their small-scale counterparts in late-type MV stellar sources, similar to what has been observed in previous studies of
274 solar flares where the power-law index, α , does not retain a constant value across all energy scales⁵²⁻⁵⁴. Hence, it is important
275 to examine the power-law indices associated with nanoflare activity across a wide range of MV spectral sub-types in order to
276 better understand the role convection plays in the generation of nanoflares.

277 Once the larger-scale flare signatures had been identified, they were subsequently removed from the time series using an
278 interval of ± 5 minutes (± 25 datapoints) from the first and last detection above the 3σ threshold. The number of macroscopic
279 flares removed were used to calculate approximate flare rates for the M stars. The lightcurves were then normalised on a
280 night by night basis, by the subtraction of a linear line of best fit. To ensure these MV stars had similar activity levels, their
281 stellar rotations periods were examined. The stellar rotation period can be estimated with Lomb-Scargle periodograms^{55,56}
282 This utilises a Fourier transform to calculate the relative power of periodic signatures in a timeseries. A normalised power
283 of 1.0 would indicate a fully periodic signal, whereas 0.0 would be a signal with no periodic nature. In practice, any signal

greater than 0.1 is a possible periodic signature. Periods in the range 1-30 days were searched for, using a ‘frequency-grid’ of 20,000 evenly spaced candidate periods (following the procedure utilised by⁵⁶ to identify periods in NGTS stellar timeseries). Common observation aliases such as the day/night cycle, and the lunar cycle were ignored, along with the harmonics of those periods. The majority of the stars did not exhibit candidate rotation periods less than 30 days, indicating they belong to the same population of slow-rotating stars, and hence had similar activity properties. Only the M2V star NGTS J045136.3-321720 deviated from this, with a possible rotation period of ~ 21 days. While the associated macroscopic flare activity was elevated with respect to the other partially convective stars (see Table 5), this star still exhibited lower activity than any fully-convective star. Additionally, it exhibited no associated nanoflare activity. As such, this possible increased rotation rate was deemed acceptable.

To ensure consistency with previous stellar nanoflare investigations, the filtering steps employed were identical to those used in⁸, with the filtered lightcurves subsequently cropped to 97 060 datapoints each to match the number statistics from the previous study. This allows a direct comparison to be made with the work of⁸, since the previously published nanoflare simulations could be re-used due to identical number statistics, filtering techniques, desired α (power-law index) and τ (e -folding time) ranges, in addition to specific NGTS-modelled noise characteristics.

Statistical and Fourier Analysis

Statistical and Fourier analysis were applied to the lightcurves following the normalisation described above, i.e., following flare removal, and detrending. This ensured the input lightcurve is comprised solely of shot and readout noise^{57,58}, alongside the background small-scale (nanoflare) stellar activity. These techniques have previously been ‘null-tested’⁸ ensuring that identically processed A-type and low activity K-type stars do not exhibit the same statistical and Fourier signatures associated with nanoflare activity. This ensured that these statistical and Fourier signatures of nanoflare activity were not a result of the processing itself.

The statistical analyses examines intensity fluctuations in the seemingly quiescent time series following traditional Z-scores approaches⁵⁹. To obtain the intensity fluctuations, each lightcurve is first detrended by a low-order polynomial so the mean value is zero. Then the time series is subsequently renormalized by its own standard deviation, σ_N . Next, a histogram of the fluctuations is generated, with deviations away from a standardised Gaussian distribution identified and compared with those associated with known nanoflare activity.

Flares are found to exhibit two distinct statistical signatures^{8,14,60,61}. First is a negative median offset, whereby the median value of the histogram is $< 0 \sigma_N$, i.e., offset from the mean of the distribution that is equal to $0 \sigma_N$ following the polynomial detrending. This is a characteristic signal associated with an exponentially decaying lightcurve, i.e., the decay phase following an impulsive deposition of energy occurs over a longer timescale, hence providing more negative fluctuations that are beneath the elevated signal mean caused by the impulsive event itself. The second nanoflare signature is an excess of fluctuations at $\sim 2 \sigma_N$, which is caused by the impulsive nature of the nanoflare energy release. This gives rise to an asymmetric distribution with an excess of fluctuations visible at $\sim 2 \sigma_N$ in the corresponding histogram, which can be further benchmarked using Fisher skewness coefficients.

Therefore, a seemingly quiescent lightcurve exhibiting both of these statistical signals is a strong candidate to contain embedded nanoflare signatures. If no nanoflare signal was present, the embedded noise fluctuations would follow a standard Gaussian distribution as a result of Poisson statistics tending to a Gaussian in the limit of large number statistics⁶⁰. In the case of very weak nanoflare activity, only a negative median offset would be present, since the weak impulsive signatures are too faint to provide a fluctuation excess at $\sim 2 \sigma_N$ in the corresponding distribution. In addition to the primary nanoflare indicators described above, we also provide benchmarks on the shapes and widths of the intensity fluctuation distributions through calculation of the kurtosis and ζ values, where ζ is the ratio of the full-width at eighth-maximum to that of the full-width at half-maximum (i.e., $\text{FW}_{\frac{1}{8}\text{M}}$ -to-FWHM ratio) of the resulting distribution. Note that a Gaussian distribution will have $\zeta = 1.73$, hence deviations from this provide an indication of the intensity fluctuation occurrences taking place close to, and far away from the time series mean.

Following on from the statistical analyses,⁸ employed Fourier techniques to identify the quasi-periodicities of stellar nanoflares, which allows for further parameterization of the embedded nanoflare activity levels. As highlighted previously⁸, the examination of Fourier signatures, which are derived directly from the stellar lightcurves, can help disambiguate any derived nanoflare characteristics and further substantiate the evidence for specific activity levels. Power spectral densities (PSDs) were derived from the stellar time series using conventional methods^{62,63}. A trendline was established over ± 6 frequency elements (± 0.239 mHz). This revealed power peaks in the same frequency range ($\sim 1 - 10$ mHz) as previously interpreted p -mode signatures^{20,21,64}, despite being a consequence of embedded nanoflare activity. Additionally, the PSDs displayed a prominent spectral slope following the peak energy value, which was also found to be due to the underlying nanoflare signal. There was an associated turning point, the frequency at which the spectral slope began to become evident, and an initial power-peak was found. These features were a further characteristic nanoflare signal.

338 The statistical and Fourier signatures were reported for each star. These properties were averaged per spectral type, by
339 using a bootstrap average. The IDL package `bootstrap_mean.pro` was used, with 1000 bootstrap resamples, and a confidence
340 interval of 0.68.

341 Monte-Carlo Nanoflare Simulation

342 To substantiate the observational findings, simulated nanoflare time series were subjected to the same statistical and Fourier
343 analyses. The 1-D simulations consisted of artificial Poisson background noise (tuned to match the observational noise
344 properties of the NGTS) alongside simulated nanoflare signals. The simulated nanoflares were generated using a wide spectrum
345 of α (power-law index) and τ (e -folding time) values, which allowed for a dense grid of possible nanoflare conditions to be
346 assimilated. The input power-law α was varied in steps of 0.05 from $1 \leq \alpha \leq 4$. The τ value was varied from $5 \leq \tau \leq 500$ s in
347 steps of 5 s. This created an input grid of 6100 possible nanoflare conditions. The resulting simulated time series appeared
348 quiescent and were therefore visually indistinguishable from the observational lightcurves, although they contained embedded
349 nanoflare signatures that could be used to benchmark the level of nanoflare activity in the observations. Each of the 6100
350 Monte-Carlo noise simulations were matched to the same 97 060 datapoints to ensure consistent number statistics with the
351 observational dataset. The same normalisation steps applied to the observational data were applied to the modelled timeseries,
352 i.e., 3σ threshold ‘flare’ subtraction, low order polynomial detrending, and the z-score normalisation. These Monte-Carlo
353 models were first developed for previous stellar nanoflare analysis⁸, and fully described therein. The nanoflare modelling
354 techniques were originally adapted from 2-D Solar nanoflare modelling code, which have been documented extensively¹⁴.

355 The nanoflare simulation requires several key input parameters. A simple flare model forms the basis of these simulations.
356 The flare begins with an impulsive energy deposition followed by approximately exponential decay. The α and τ values will
357 dictate the frequency of energy release, and the time taken for the flare to decay. The modelled flare-decay rate, τ was varied
358 by $\pm 10\%$ in each simulated timeseries. These decay rates are a function of the underlying plasma conditions, and hence are
359 not consistent over time. A variation of $\pm 10\%$ allows for a more realistic representation of the approximately exponential
360 decay timescales. The energy range of nanoflares spanned $10^{22} - 10^{25}$ ergs. These flare energies are generated using a random
361 power-law generation function. This will randomly order energy values according to the input power-law index, α . These
362 events are then ‘decayed’ via an exponential decay with the characteristic timescale being within $\pm 10\%$ of the input τ value.
363 The power-law distribution only gives information about the relative frequency and energy release of flare events, but does not
364 provide the number of occurrences of these events. As such, the number of flare events needs to be normalised, ensuring a
365 given power-law index leads to the correct flare energy release rate. This normalisation is achieved through comparison with
366 the work of⁶ and^{65, 65} find that for an energy of 10^{25} ergs, the expected flare frequency is $\sim 2000 \times 10^{-50} \text{ erg}^{-1} \text{ cm}^{-2} \text{ s}^{-1}$. This
367 allows an approximate lower-limit to the number of flare events to be set. This normalisation requires the underlying stellar
368 area. As these stars are point-sources, the simulated area was the entire Earth-facing area of the star. This was set to $\sim 10^{21} \text{ cm}^2$
369. This is the approximate surface area of an M-dwarf⁶⁶. While larger flares are reliant on highly localised and intense magnetic
370 conditions, nanoflares are expected to occur continuously throughout the entire stellar atmosphere. As such, the entire stellar
371 surface may be treated as a source of nanoflare activity. Combined with an exposure time and cadence matched to observation
372 (i.e., 10 seconds, and 12 seconds respectively for the NGTS), the number of nanoflare events per second were normalised
373 for each simulation. A direct one-to-one scaling was used to convert the flare energies into ‘counts’. The whitelight NGTS
374 observations capture the majority of the flare energy, as flares (particularly M-dwarf flares⁶⁷) emit strongly in whitelight and
375 at UV wavelengths^{68, 69}. The flare energies themselves are assumed to scale linearly with area⁴³. As such, we convert our
376 simulated flare energies directly into counts. A ‘ 1σ ’ flare energy is used to ‘normalise’ this conversion. This is an estimate of
377 the flare energy corresponding to a 1σ fluctuation. This requires a degree of estimation, and is dependent on the underlying
378 observation platform. This should be set to the approximate energy level of the noise floor, i.e., the energy of an event within
379 the noise floor. A value in the range $10^{24} - 10^{25}$ ergs would set the noise floor at the upper span of nanoflaring energies, an
380 appropriate estimate for most observation systems, as these nanoflares remain on or below the noise-floor. The value of 5×10^{24}
381 ergs was used as the 1σ value in this work. This energy ensures that the span of these nanoflare fluctuations remain within the
382 noise envelope, with a maximum fluctuation of 2.5σ at the upper energy of 10^{25} ergs. This ensures that the modelled timeseries
383 remain seemingly ‘quiescent’, matching it to their companion observational timeseries.

384 The statistical and Fourier signatures of these simulated timeseries were output as 2-D ‘heat-maps’, allowing direct
385 comparison between observed and simulated statistical and Fourier properties, to diagnose the underlying nanoflare conditions.

386 While efforts were made to match as many properties to the original study (to ensure consistent number statistics), there was
387 a slight deviation in the Fourier analysis. The longest continuous time series (i.e., the longest uninterrupted series of frames)
388 common to the observed stars in this study was 2095 datapoints, slightly shorter than the 2316 consecutive frames employed
389 by⁸. This resulted in the frequency resolution being slightly reduced from $\Delta f = 0.0356$ mHz to $\Delta f = 0.0398$ mHz in the
390 present study. In order to readily compare the observational PSDs to those calculated from the Monte Carlo nanoflare models,
391 the Fourier signatures needed to be re-calculated adhering to the new frequency resolution. Hence, utilising the new frequency

392 resolution, we re-computed the PSDs and corresponding ‘heat map’ of the simulated Fourier properties as a function of both
 393 the nanoflare power-law and e -folding time. The recalculated heat map is displayed in Figure 5. Due to the change in frequency
 394 resolution being a relatively small value (0.0042 mHz), no noticeable deviations from Figure 5 and the original distribution can
 395 be seen, with the trends identical in both studies. This is likely a result of the Fourier nanoflare trends being relatively broad in
 396 frequency with peak values sufficiently away from the lowest and highest (i.e., Nyquist) frequencies of the time series, hence
 397 are not significantly affected by very small changes in the underlying frequency resolution.

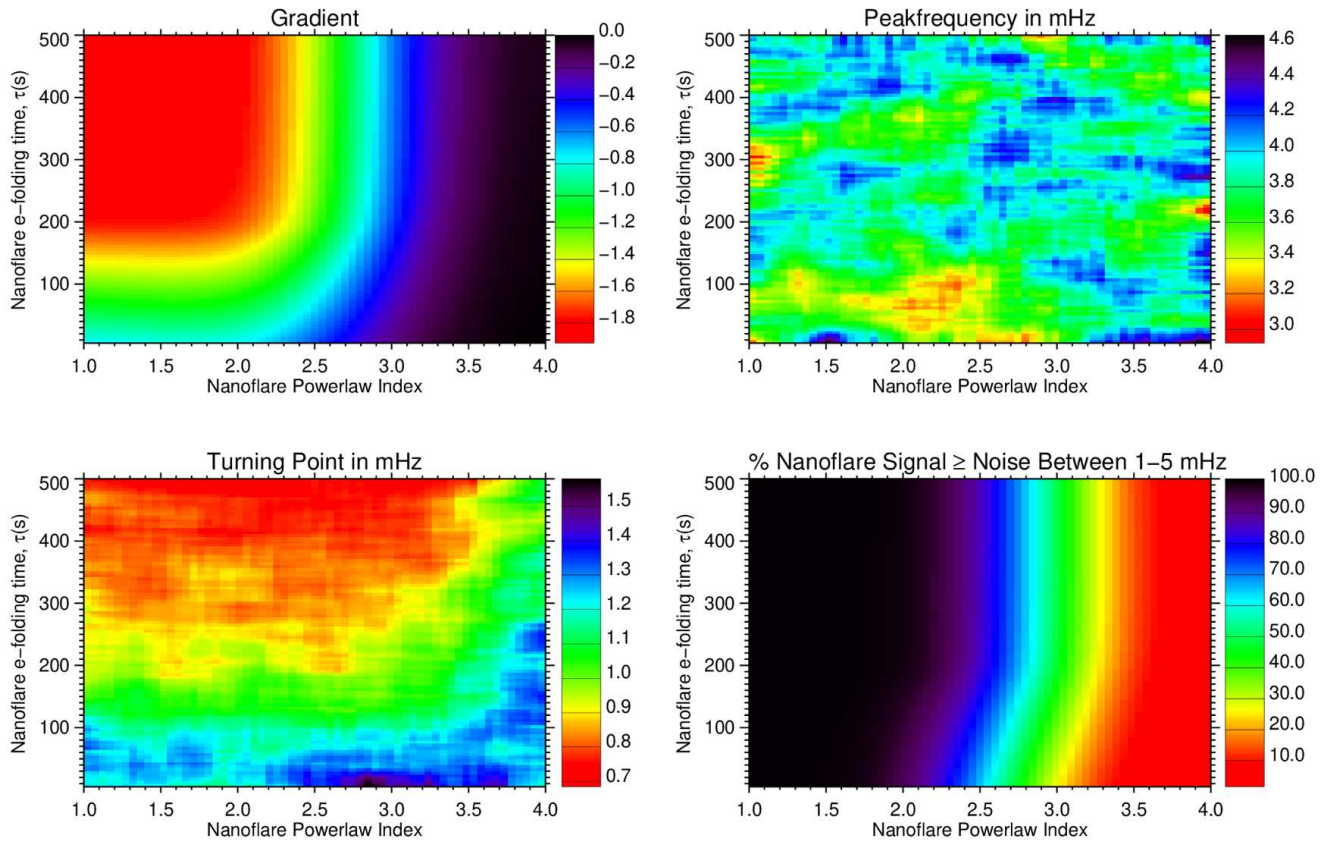


Figure 5. A reproduction of Figure 7 from⁸, with the constituent PSDs re-calculated for 2095 datapoints to match the longest continuous time series used in the present study. The primary peak frequencies (lower-left), spectral slopes (upper-left), dominant frequencies following detrending (upper-right), and the percentage of nanoflare power above the noise floor in the range of 1 – 5 mHz (lower-right), is displayed as a function of the power-law index, α , and the decay timescale, τ , used to generate the synthetic time series. While a few individual values differ, the overall trends and the magnitude of the derived signals are consistent with the PSD properties generated from 2316 data points⁸.

398 References

- 399 1. Priest, E. R. Role of magnetic reconnection in solar flares. *Adv. Space Res.* **6**, 73–82, DOI: [10.1016/0273-1177\(86\)90120-1](https://doi.org/10.1016/0273-1177(86)90120-1)
 400 (1986).
- 401 2. Reale, F. Diagnostics of stellar flares from X-ray observations: from the decay to the rise phase. *Astron. Astrophys.* **471**,
 402 271–279, DOI: [10.1051/0004-6361:20077223](https://doi.org/10.1051/0004-6361:20077223) (2007). [0705.3254](https://arxiv.org/abs/0705.3254).
- 403 3. Cargill, P. J., Warren, H. P. & Bradshaw, S. J. Modelling nanoflares in active regions and implications for coronal heating
 404 mechanisms. *Philos. Transactions Royal Soc. Lond. Ser. A* **373**, 20140260–20140260, DOI: [10.1098/rsta.2014.0260](https://doi.org/10.1098/rsta.2014.0260)
 405 (2015).
- 406 4. Cargill, P. J. & Klimchuk, J. A. Nanoflare Heating of the Corona Revisited. *Astrophys. J.* **605**, 911–920, DOI: [10.1086/
 407 382526](https://doi.org/10.1086/382526) (2004).

- 408 5. Antiochos, S. K. & Sturrock, P. A. Evaporative cooling of flare plasma. *Astrophys. J.* **220**, 1137–1143, DOI: [10.1086/155999](https://doi.org/10.1086/155999)
409 (1978).
- 410 6. Aschwanden, M. J. *et al.* Time Variability of the “Quiet” Sun Observed with TRACE. II. Physical Parameters, Temperature
411 Evolution, and Energetics of Extreme-Ultraviolet Nanoflares. *Astrophys. J.* **535**, 1047–1065, DOI: [10.1086/308867](https://doi.org/10.1086/308867) (2000).
- 412 7. Parker, E. N. Nanoflares and the Solar X-Ray Corona. *Astrophys. J.* **330**, 474, DOI: [10.1086/166485](https://doi.org/10.1086/166485) (1988).
- 413 8. Dillon, C. J. *et al.* Statistical Signatures of Nanoflare Activity. II. A Nanoflare Explanation for Periodic Brightenings in
414 Flare Stars Observed by NGTS. *Astrophys. J.* **904**, 109, DOI: [10.3847/1538-4357/abbfa8](https://doi.org/10.3847/1538-4357/abbfa8) (2020). [2010.04167](https://arxiv.org/abs/2010.04167).
- 415 9. Klimchuk, J. A. On solving the coronal heating problem. *Sol. Phys.* **234**, 41–77, DOI: [10.1007/s11207-006-0055-z](https://doi.org/10.1007/s11207-006-0055-z) (2006).
- 416 10. Benz, A. O. Flare observations. *Living Rev. Sol. Phys.* **14**, 2, DOI: [10.1007/s41116-016-0004-3](https://doi.org/10.1007/s41116-016-0004-3) (2016).
- 417 11. Hudson, H. S. Solar flares, microflares, nanoflares, and coronal heating. *Sol. Phys.* **133**, 357–369, DOI: [10.1007/
418 BF00149894](https://doi.org/10.1007/BF00149894) (1991).
- 419 12. Aschwanden, M. J. Do EUV Nanoflares Account for Coronal Heating? *Sol. Phys.* **190**, 233–247, DOI: [10.1023/A:
420 1005288725034](https://doi.org/10.1023/A:1005288725034) (1999).
- 421 13. Aschwanden, M. J., Winebarger, A., Tsiklauri, D. & Peter, H. The Coronal Heating Paradox. *Astrophys. J.* **659**, 1673–1681,
422 DOI: [10.1086/513070](https://doi.org/10.1086/513070) (2007).
- 423 14. Jess, D. B. *et al.* Statistical Signatures of Nanoflare Activity. I. Monte Carlo Simulations and Parameter-space Exploration.
424 *Astrophys. J.* **871**, 133, DOI: [10.3847/1538-4357/aaf8ae](https://doi.org/10.3847/1538-4357/aaf8ae) (2019). [1812.06978](https://arxiv.org/abs/1812.06978).
- 425 15. Mullan, D. J. & Houdebine, E. R. A Transition of Dynamo Modes in M Dwarfs: Narrowing Down the Spectral Range
426 Where the Transition Occurs. *Astrophys. J.* **891**, 128, DOI: [10.3847/1538-4357/ab6ffa](https://doi.org/10.3847/1538-4357/ab6ffa) (2020). [2001.08721](https://arxiv.org/abs/2001.08721).
- 427 16. Efron, B. *et al.* Bootstrap methods: Another look at the jackknife. *Annals Stat.* **7**, 1–26 (1979).
- 428 17. Simpson, G. & Mayer-Hasselwander, H. Bootstrap sampling - Applications in gamma-ray astronomy. *Astron. Astrophys.*
429 **162**, 340–348 (1986).
- 430 18. Desmars, J., Arlot, S., Arlot, J. E., Lainey, V. & Vienne, A. Estimating the accuracy of satellite ephemerides using the
431 bootstrap method. *Astron. Astrophys.* **499**, 321–330, DOI: [10.1051/0004-6361/200811509](https://doi.org/10.1051/0004-6361/200811509) (2009).
- 432 19. Yao, J. M., Manchester, R. N. & Wang, N. Determination of the Sun’s offset from the Galactic plane using pulsars. *Mon.*
433 *Not. R. Astron. Soc.* **468**, 3289–3294, DOI: [10.1093/mnras/stx729](https://doi.org/10.1093/mnras/stx729) (2017). [1704.01272](https://arxiv.org/abs/1704.01272).
- 434 20. Rodríguez-López, C., MacDonald, J., Amado, P. J., Moya, A. & Mullan, D. The theoretical instability strip of M dwarf
435 stars. *Mon. Not. R. Astron. Soc.* **438**, 2371–2379, DOI: [10.1093/mnras/stt2352](https://doi.org/10.1093/mnras/stt2352) (2014). [1312.2743](https://arxiv.org/abs/1312.2743).
- 436 21. Rodríguez, E. *et al.* Search for pulsations in M dwarfs in the Kepler short-cadence data base. *Mon. Not. R. Astron. Soc.*
437 **457**, 1851–1863, DOI: [10.1093/mnras/stw033](https://doi.org/10.1093/mnras/stw033) (2016).
- 438 22. Guenther, D. B. *et al.* The Nature of p-Modes and Granulation in Procyon: New MOST Photometry and New Yale
439 Convection Models. *Astrophys. J.* **687**, 1448–1459, DOI: [10.1086/592060](https://doi.org/10.1086/592060) (2008).
- 440 23. Pedersen, M. G. *et al.* Do A-type stars flare? *Mon. Not. R. Astron. Soc.* **466**, 3060–3076, DOI: [10.1093/mnras/stw3226](https://doi.org/10.1093/mnras/stw3226)
441 (2017). [1612.04575](https://arxiv.org/abs/1612.04575).
- 442 24. Spiegel, E. A. & Zahn, J. P. The solar tachocline. *Astron. Astrophys.* **265**, 106–114 (1992).
- 443 25. Parfrey, K. P. & Menou, K. The Origin of Solar Activity in the Tachocline. *Astrophys. J. Lett.* **667**, L207–L210, DOI:
444 [10.1086/522426](https://doi.org/10.1086/522426) (2007). [0708.3675](https://arxiv.org/abs/0708.3675).
- 445 26. Durney, B. R., De Young, D. S. & Roxburgh, I. W. On the Generation of the Largescale and Turbulent Magnetic Fields in
446 the Solar Type Stars. *Sol. Phys.* **145**, 207–225, DOI: [10.1007/BF00690652](https://doi.org/10.1007/BF00690652) (1993).
- 447 27. Browning, M. K. Simulations of Dynamo Action in Fully Convective Stars. *Astrophys. J.* **676**, 1262–1280, DOI:
448 [10.1086/527432](https://doi.org/10.1086/527432) (2008). [0712.1603](https://arxiv.org/abs/0712.1603).
- 449 28. Pipin, V. V. & Seehafer, N. Stellar dynamos with $\omega \times j$ effect. *A@AND@A* **493**, 819–828, DOI: [10.1051/0004-6361:
450 200810766](https://doi.org/10.1051/0004-6361:200810766) (2009).
- 451 29. Wright, N. J. & Drake, J. J. Solar-type dynamo behaviour in fully convective stars without a tachocline. *Nature* **535**,
452 526–528, DOI: [10.1038/nature18638](https://doi.org/10.1038/nature18638) (2016). [1607.07870](https://arxiv.org/abs/1607.07870).
- 453 30. Wright, N. J., Newton, E. R., Williams, P. K. G., Drake, J. J. & Yadav, R. K. The stellar rotation-activity relationship in
454 fully convective M dwarfs. *Mon. Not. R. Astron. Soc.* **479**, 2351–2360, DOI: [10.1093/mnras/sty1670](https://doi.org/10.1093/mnras/sty1670) (2018). [1807.03304](https://arxiv.org/abs/1807.03304).

- 455 **31.** Tsuneta, S. & Katsukawa, Y. *Coronal Heating with Sweet-Parker Picoflares*, vol. 325 of *Astronomical Society of the Pacific*
456 *Conference Series*, 289 (2004).
- 457 **32.** Mohanty, S., Basri, G., Shu, F., Allard, F. & Chabrier, G. Activity in Very Cool Stars: Magnetic Dissipation in Late M and
458 L Dwarf Atmospheres. *Astrophys. J.* **571**, 469–486, DOI: [10.1086/339911](https://doi.org/10.1086/339911) (2002). [astro-ph/0201518](https://arxiv.org/abs/astro-ph/0201518).
- 459 **33.** Loureiro, N. F. & Uzdensky, D. A. Magnetic reconnection: from the Sweet-Parker model to stochastic plasmoid chains.
460 *Plasma Phys. Control. Fusion* **58**, 014021, DOI: [10.1088/0741-3335/58/1/014021](https://doi.org/10.1088/0741-3335/58/1/014021) (2016). [1507.07756](https://arxiv.org/abs/1507.07756).
- 461 **34.** Takahashi, H. R., Kudoh, T., Masada, Y. & Matsumoto, J. Scaling Law of Relativistic Sweet-Parker-type Magnetic
462 Reconnection. *Astrophys. J. Lett.* **739**, L53, DOI: [10.1088/2041-8205/739/2/L53](https://doi.org/10.1088/2041-8205/739/2/L53) (2011). [1108.3891](https://arxiv.org/abs/1108.3891).
- 463 **35.** Tenerani, A., Velli, M., Rappazzo, A. F. & Pucci, F. Magnetic Reconnection: Recursive Current Sheet Collapse Triggered
464 by “Ideal” Tearing. *Astrophys. J. Lett.* **813**, L32, DOI: [10.1088/2041-8205/813/2/L32](https://doi.org/10.1088/2041-8205/813/2/L32) (2015). [1506.08921](https://arxiv.org/abs/1506.08921).
- 465 **36.** Shi, C., Velli, M. & Tenerani, A. Marginal Stability of Sweet-Parker Type Current Sheets at Low Lundquist Numbers.
466 *Astrophys. J.* **859**, 83, DOI: [10.3847/1538-4357/aabd83](https://doi.org/10.3847/1538-4357/aabd83) (2018). [1802.07162](https://arxiv.org/abs/1802.07162).
- 467 **37.** Papini, E., Landi, S. & Del Zanna, L. Fast Magnetic Reconnection: Secondary Tearing Instability and Role of the Hall
468 Term. *Astrophys. J.* **885**, 56, DOI: [10.3847/1538-4357/ab4352](https://doi.org/10.3847/1538-4357/ab4352) (2019). [1906.06779](https://arxiv.org/abs/1906.06779).
- 469 **38.** Ricker, G. R. *et al.* Transiting Exoplanet Survey Satellite (TESS). In *Proc. SPIE*, vol. 9143 of *Society of Photo-Optical*
470 *Instrumentation Engineers (SPIE) Conference Series*, 914320, DOI: [10.1117/12.2063489](https://doi.org/10.1117/12.2063489) (2014). [1406.0151](https://arxiv.org/abs/1406.0151).
- 471 **39.** Dhillon, V. S. *et al.* HiPERCAM: a high-speed quintuple-beam CCD camera for the study of rapid variability in the
472 universe. In *Proc. SPIE*, vol. 9908 of *Society of Photo-Optical Instrumentation Engineers (SPIE) Conference Series*,
473 99080Y, DOI: [10.1117/12.2229055](https://doi.org/10.1117/12.2229055) (2016). [1606.09214](https://arxiv.org/abs/1606.09214).
- 474 **40.** Antonelli, L. A. The rem telescope: a robotic facility to promptly follow-up grbs and cosmic fast transients. *AIP Conf.*
475 *Proc.* **797**, 173–180, DOI: [10.1063/1.2130230](https://doi.org/10.1063/1.2130230) (2005). <https://aip.scitation.org/doi/pdf/10.1063/1.2130230>.
- 476 **41.** Wheatley, P. J. *et al.* The Next Generation Transit Survey (NGTS). *Mon. Not. R. Astron. Soc.* **475**, 4476–4493, DOI:
477 [10.1093/mnras/stx2836](https://doi.org/10.1093/mnras/stx2836) (2018). [1710.11100](https://arxiv.org/abs/1710.11100).
- 478 **42.** Stassun, K. G. *et al.* The TESS Input Catalog and Candidate Target List. *Astron. J.* **156**, 102, DOI: [10.3847/1538-3881/](https://doi.org/10.3847/1538-3881/aad050)
479 [aad050](https://doi.org/10.3847/1538-3881/aad050) (2018). [1706.00495](https://arxiv.org/abs/1706.00495).
- 480 **43.** Yang, H. *et al.* The flaring activity of m dwarfs in the kepler field. *The Astrophys. J.* **849**, 36, DOI: [10.3847/1538-4357/](https://doi.org/10.3847/1538-4357/aa8ea2)
481 [aa8ea2](https://doi.org/10.3847/1538-4357/aa8ea2) (2017).
- 482 **44.** Hawley, S. L. *et al.* Kepler Flares. I. Active and Inactive M Dwarfs. *Astrophys. J.* **797**, 121, DOI: [10.1088/0004-637X/797/](https://doi.org/10.1088/0004-637X/797/2/121)
483 [2/121](https://doi.org/10.1088/0004-637X/797/2/121) (2014). [1410.7779](https://arxiv.org/abs/1410.7779).
- 484 **45.** Robinson, R. D., Carpenter, K. G., Percival, J. W. & Bookbinder, J. A. A Search for Microflaring Activity on dMe Flare
485 Stars. I. Observations of the dM8e Star CN Leonis. *Astrophys. J.* **451**, 795, DOI: [10.1086/176266](https://doi.org/10.1086/176266) (1995).
- 486 **46.** Robinson, R. D., Carpenter, K. G. & Percival, J. W. A Search for Microflaring Activity on DME Flare Stars. II. Observations
487 of YZ Canis Minoris. *Astrophys. J.* **516**, 916–923, DOI: [10.1086/307133](https://doi.org/10.1086/307133) (1999).
- 488 **47.** Kashyap, V. L., Drake, J. J., Güdel, M. & Audard, M. Flare Heating in Stellar Coronae. *Astrophys. J.* **580**, 1118–1132,
489 DOI: [10.1086/343869](https://doi.org/10.1086/343869) (2002). [astro-ph/0208546](https://arxiv.org/abs/astro-ph/0208546).
- 490 **48.** Güdel, M., Audard, M., Kashyap, V. L., Drake, J. J. & Guinan, E. F. Are coronae of magnetically active stars heated by
491 flares? II. extreme ultraviolet and x-ray flare statistics and the differential emission measure distribution. *The Astrophys. J.*
492 **582**, 423–442, DOI: [10.1086/344614](https://doi.org/10.1086/344614) (2003).
- 493 **49.** Güdel, M. X-ray astronomy of stellar coronae. *Astron. Astrophys. Rev.* **12**, 71–237, DOI: [10.1007/s00159-004-0023-2](https://doi.org/10.1007/s00159-004-0023-2)
494 (2004). [astro-ph/0406661](https://arxiv.org/abs/astro-ph/0406661).
- 495 **50.** Welsh, B. Y. *et al.* GALEX high time-resolution ultraviolet observations of dMe flare events. *Astron. Astrophys.* **458**,
496 921–930, DOI: [10.1051/0004-6361:20065304](https://doi.org/10.1051/0004-6361:20065304) (2006). [astro-ph/0608254](https://arxiv.org/abs/astro-ph/0608254).
- 497 **51.** Reale, F. Plasma Sloshing in Pulse-heated Solar and Stellar Coronal Loops. *Astrophys. J. Lett.* **826**, L20, DOI: [10.3847/](https://doi.org/10.3847/2041-8205/826/2/L20)
498 [2041-8205/826/2/L20](https://doi.org/10.3847/2041-8205/826/2/L20) (2016). [1607.01329](https://arxiv.org/abs/1607.01329).
- 499 **52.** Wang, F. Y. & Dai, Z. G. Self-organized criticality in X-ray flares of gamma-ray-burst afterglows. *Nat. Phys.* **9**, 465–467,
500 DOI: [10.1038/nphys2670](https://doi.org/10.1038/nphys2670) (2013). [1308.1253](https://arxiv.org/abs/1308.1253).
- 501 **53.** Ryan, D. F., Dominique, M., Seaton, D., Stegen, K. & White, A. Effects of flare definitions on the statistics of derived flare
502 distributions. *Astron. Astrophys.* **592**, A133, DOI: [10.1051/0004-6361/201628130](https://doi.org/10.1051/0004-6361/201628130) (2016). [1606.04472](https://arxiv.org/abs/1606.04472).

- 503 **54.** Milligan, R. O., Hudson, H. S., Chamberlin, P. C., Hannah, I. G. & Hayes, L. A. Lyman-alpha Variability During Solar
504 Flares Over Solar Cycle 24 Using GOES-15/EUVS-E. *Space Weather*. **18**, e02331, DOI: [10.1029/2019SW002331](https://doi.org/10.1029/2019SW002331) (2020).
505 [1910.01364](https://doi.org/10.1029/2019SW002331).
- 506 **55.** VanderPlas, J. T. Understanding the lomb–scargle periodogram. *The Astrophys. J. Suppl. Ser.* **236**, 16, DOI: [10.3847/](https://doi.org/10.3847/1538-4365/aab766)
507 [1538-4365/aab766](https://doi.org/10.3847/1538-4365/aab766) (2018).
- 508 **56.** Jackman, J. A. G. *et al.* Stellar flares detected with the Next Generation Transit Survey. *Mon. Not. R. Astron. Soc.* **504**,
509 3246–3264, DOI: [10.1093/mnras/stab979](https://doi.org/10.1093/mnras/stab979) (2021). [2104.02648](https://doi.org/10.1093/mnras/stab979).
- 510 **57.** Terrell, J. Size limits on fluctuating astronomical sources. *Astrophys. J. Lett.* **213**, L93–L97, DOI: [10.1086/182417](https://doi.org/10.1086/182417) (1977).
- 511 **58.** Delouille, V., Chainais, P. & Hochedez, J. F. Spatial and Temporal Noise in Solar EUV Observations. *Sol. Phys.* **248**,
512 441–455, DOI: [10.1007/s11207-008-9131-x](https://doi.org/10.1007/s11207-008-9131-x) (2008).
- 513 **59.** Sprinthal, R. *Basic Statistical Analysis* (Prentice Hall, 1990).
- 514 **60.** Terzo, S. *et al.* Widespread Nanoflare Variability Detected with Hinode/X-Ray Telescope in a Solar Active Region.
515 *Astrophys. J.* **736**, 111, DOI: [10.1088/0004-637X/736/2/111](https://doi.org/10.1088/0004-637X/736/2/111) (2011). [1105.2506](https://doi.org/10.1088/0004-637X/736/2/111).
- 516 **61.** Jess, D. B., Mathioudakis, M. & Keys, P. H. Nanoflare Activity in the Solar Chromosphere. *Astrophys. J.* **795**, 172, DOI:
517 [10.1088/0004-637X/795/2/172](https://doi.org/10.1088/0004-637X/795/2/172) (2014). [1409.6726](https://doi.org/10.1088/0004-637X/795/2/172).
- 518 **62.** Welch, P. D. A direct digital method of power spectrum estimation. *IBM J. Res. Dev.* **5**, 141–156, DOI: [10.1147/rd.52.0141](https://doi.org/10.1147/rd.52.0141)
519 (1961).
- 520 **63.** Vaughan, S. Random time series in astronomy. *Philos. Transactions Royal Soc. Lond. Ser. A* **371**, 20110549–20110549,
521 DOI: [10.1098/rsta.2011.0549](https://doi.org/10.1098/rsta.2011.0549) (2012).
- 522 **64.** Andrews, A. D. Investigation of micro-flaring and secular and quasi-periodic variations in dMe flare stars. I. Suspected
523 ultra-short “waves” in the dM2–3estars V1285 Aquilae. *Astron. Astrophys.* **210**, 303–310 (1989).
- 524 **65.** Parnell, C. E. & Jupp, P. E. Statistical Analysis of the Energy Distribution of Nanoflares in the Quiet Sun. *Astrophys. J.*
525 **529**, 554–569, DOI: [10.1086/308271](https://doi.org/10.1086/308271) (2000).
- 526 **66.** Reid, I. N. & Hawley, S. L. *New light on dark stars : red dwarfs, low-mass stars, brown dwarfs* (Springer-Verlag Berlin
527 Heidelberg, 2005).
- 528 **67.** Walkowicz, L. M. *et al.* White-light Flares on Cool Stars in the Kepler Quarter 1 Data. *Astron. J.* **141**, 50, DOI:
529 [10.1088/0004-6256/141/2/50](https://doi.org/10.1088/0004-6256/141/2/50) (2011). [1008.0853](https://doi.org/10.1088/0004-6256/141/2/50).
- 530 **68.** Woods, T. N., Kopp, G. & Chamberlin, P. C. Contributions of the solar ultraviolet irradiance to the total solar irradiance
531 during large flares. *J. Geophys. Res. (Space Physics)* **111**, A10S14, DOI: [10.1029/2005JA011507](https://doi.org/10.1029/2005JA011507) (2006).
- 532 **69.** Schmitt, J. H. M. M., Kanbach, G., Rau, A. & Steinle, H. Optical microflaring on the nearby flare star binary UV Ceti.
533 *Astron. Astrophys.* **589**, A48, DOI: [10.1051/0004-6361/201628199](https://doi.org/10.1051/0004-6361/201628199) (2016).

534 Acknowledgements

535 C.J.D., D.B.J. and S.D.T.G. wish to thank Invest NI and Radox Laboratories Ltd. for the award of a Research and Development
536 Grant (059RDEN-1) that allowed the computational techniques employed to be developed. D.B.J. would like to thank the
537 UK Science and Technology Facilities Council (STFC) for an Ernest Rutherford Fellowship (ST/K004220/1), in addition to a
538 dedicated standard grant (ST/L002744/1) that allowed this project to be started. D.B.J. and M.M. would like to thank STFC
539 for the consolidated grant ST/T00021X/1. J.A.G.J. acknowledges support from grant HST-GO-15955.004-A from the Space
540 Telescope Science Institute, which is operated by the Association of Universities for Research in Astronomy, Inc., under NASA
541 contract NAS 5-26555 S.L.C would like to thank STFC for an Ernest Rutherford Fellowship (ST/R003726/1). P.J.W., D.R.A.,
542 and R.G.W. acknowledge support from STFC consolidated grants ST/L000733/1 and ST/P000495/1. This project is based
543 on data collected under the NGTS project at the ESO La Silla Paranal Observatory. The NGTS facility is operated by the
544 consortium institutes with support from the UK STFC under projects ST/M001962/1 and ST/S002642/1. D.B.J. wishes to
545 acknowledge scientific discussions with the Waves in the Lower Solar Atmosphere (WaLSA; www.WaLSA.team) team, which
546 is supported by the Research Council of Norway (project no. 262622) and the Royal Society (award no. Hooke18b/SCTM).
547 J.I.V. acknowledges support of CONICYT-PFCHA/Doctorado Nacional-21191829.

548 **Author contributions statement**

549 C.J.D, D.B.J, and M.M. conceived the experiment. C.A.W. identified the potential to observe stellar nanoflares through the use
550 of NGTS, as well as benchmarking/quality control science verification checks. C.J.D conducted the experiment and analysed
551 the results. C.J.D and D.B.J prepared the manuscript. C.A.W, J.A.G.J., P.J.W, M.R.G, S.L.C, D.R.A, M.R.B, R.G.W, and J.I.V
552 provided the observational products as part of the NGTS. All authors reviewed the manuscript, and provided input.

553 **Additional information**

554 Observational data supporting the findings of this study are available from the NGTS 2020 data release, <https://archive.eso.org/cms/eso->
555 [archive-news/second-data-release-of-the-next-generation-transit-survey.html](https://archive.eso.org/cms/eso-archive-news/second-data-release-of-the-next-generation-transit-survey.html). The processed lightcurves are available from
556 the authors upon reasonable request. The Monte-Carlo models are available from the authors, upon reasonable request. The
557 authors declare no competing interests.

Sp Type	NGTS ID	GAIA ID	TIC ID	RA	Dec	Mass (M_{\odot})	Radius (R_{\odot})	Luminosity (L_{\odot})	Distance (pc)	Approximate Flare Rate per Hour	Magnitude
M0V	NGTS J233315.1-385757	6538313140873424640	224245757	353.312913	-38.965817	0.487596	0.489513	0.04772778	100.33	0.0123635	13.10
M0V	NGTS J045221.8-312424	4874911889552910000	1310695	73.090834	-31.406834	0.597557	0.611732	0.07879962	137.421	0.0154544	13.26
M0V	NGTS J052346.3-361114	4822374303400198144	167745038	80.94287	-36.187338	0.566358	0.574022	0.07396496	123.332	0.00618174	13.04
M0V	NGTS J061346.1-362248	2885025813007881728	267248553	93.442125	-36.380098	0.585147	0.596407	0.07490093	137.363	0.0123635	13.24
M0V	NGTS J061054.6-370701	2884885281677800448	300200809	92.72739	-37.116954	0.575812	0.585163	0.06398756	112.406	0.0401813	12.99
M1V	NGTS J233248.3-382456	6538532356004046592	224244565	353.201262	-38.415564	0.542372	0.546805	0.05344092	90.7535	0.0123635	12.97
M1V	NGTS J051250.6-361938	4821058497219315328	14173066	78.210928	-36.327354	0.596268	0.61012	0.06084004	201.14	0.0123635	14.16
M1V	NGTS J052652.1-373123	4821222942926810752	192785958	81.717213	-37.523125	0.567364	0.575197	0.05580399		0.00309087	13.57
M1V	NGTS J235034.7-373312	2310510165491596672	183536494	357.644544	-37.553375	0.506923	0.509045	0.04646323	83.9291	0.00927262	12.84
M1V	NGTS J111257.7-331216	5403344977522967424	23438898	168.240279	-33.20455	0.460039	0.462724	0.03412572	73.1095	0.0185452	12.92
M2V	NGTS J045136.3-321720	4874656837214833664	1309522	72.901424	-32.288803	0.56	0.806538	0.1124733	247.955	0.0278178	14.32
M2V	NGTS J050254.6-352000	4825066629419253632	1526841	75.72729	-35.333409	0.469279	0.471581	0.03436859	69.7222	0.0185452	12.72
M2V	NGTS J051926.5-253444	2957763042671388416	30960826	79.860208	-25.578811	0.460925	0.463568	0.03302738	90.6288	0.00927262	13.49
M2V	NGTS J053614.4-353309	4821870486556489216	24612475	84.059908	-35.552443	0.501857	0.503859	0.03897486	90.6101	0.0154544	13.2
M2V	NGTS J062005.7-372555	5575203489668007936	393481864	95.023721	-37.431899	0.400268	0.407808	0.02305492	87.7167	0	13.83
M2.5V	NGTS J045008.8-362401	4818804257863710336	77369893	72.536742	-36.400372	0.545633	0.550421	0.05525498	118.868	0.0494539	13.07
M2.5V	NGTS J050359.5-305327	4876285488813663232	1439071	74.755373	-30.999599	0.456069	0.458954	0.02748212	54.6863	0.00618174	12.8
M2.5V	NGTS J045901.2-305958	4875598534564509312	1535810	75.997888	-30.890807	0.380031	0.389898	0.01965184	68.7496	0.0710901	13.65
M2.5V	NGTS J050810.8-371850	4823535318959536256	14084620	77.044884	-37.313753	0.514811	0.517217	0.03755042	59.1582	0.0309087	12.29
M2.5V	NGTS J061516.4-360818	2885223381503521536	267327257	93.818249	-36.138454	0.496041	0.497965	0.03437556	118.666	0.0278178	13.99
M3V	NGTS J035219.1-311459	4886786408973741568	166804322	58.079759	-31.249846	0.544884	0.549588	0.03602405	123.566	0.0216361	13.63
M3V	NGTS J050230.0-355301	4824660428592359552	13982951	75.624229	-35.883643	0.308218	0.327511	0.01185441	41.1162	0.00927262	13.1
M3V	NGTS J051925.5-235535	2958246827787260032	30961390	79.856241	-23.926311	0.564934	0.572365	0.04099549	131.705	0.0865444	13.94
M3V	NGTS J052116.1-322429	4826608831916384640	78053729	80.317094	-32.357958	0.401901	0.409266	0.01826787	39.3307	0.0494539	12.52
M3V	NGTS J000722.8-293528	2320750123439437184	12418184	1.845141	-29.5912	0.22872	0.257223	0.007069197	40.1093	0.0216361	13.44
M4V	NGTS J035624.7-311140	4886831592030178944	166869904	59.102836	-31.194413	0.402508	0.409808	0.01474621	37.7653	0.10509	12.7
M4V	NGTS J044312.0-322643	4874430475258301184	170882537	70.800028	-32.445142	0.512283	0.514585	0.02822354		0.0834535	12.6
M4V	NGTS J045519.0-321222	4873878176823736192	1357792	73.829291	-32.206129	0.170431	0.201449	0.003005163	21.8796	0.0865444	13.72
M4V	NGTS J050423.8-373021	4823476460727785728	14001734	76.099199	-37.505698	0.434448	0.438763	0.02066878		0.148362	12.42
M4V	NGTS J2341092-363819	2311548448064869120	224276435	355.288136	-36.638609	0.253768	0.279818	0.005977345	38.7917	0.0649083	13.79

Table 5. The Spectral type, NGTS identifier, Gaia source ID, Tess Input Catalog (TIC) ID, RA, Dec, Stellar Mass (in Solar mass units), Stellar Radius (in Solar radii units), Distance (in parsecs), Stellar Luminosity (in Solar luminosity units), and the Macroscopic Flare Rate (per hour) for the stars used in the analysis. The Stellar masses, radi. and luminosity data is from the Tess Input Catalog release V8.⁴²